Journal of Materials Chemistry A

Accepted Manuscript

ROYAL SOCIETY OF CHEMISTRY

www.rsc.org/materialsA

Cite this: DOI: 10.1039/c0xx00000x

www.rsc.org/xxxxxx

ARTICLE TYPE

Enhanced photocatalytic H_2 evolution over noble-metal-free NiS cocatalyst modified CdS nanorods/g-C_3N_4 heterojunctions

Jielin Yuan, Jiuqing Wen, Yongming, Zhong, Xin Li,* Yueping Fang,* Shengsen Zhang, Wei Liu*

Received (in XXX, XXX) Xth XXXXXXXXX 20XX, Accepted Xth XXXXXXXXX 20XX
DOI: 10.1039/b000000x

In this report, the CdS nanorods/g-C_3N_4 heterojunctions loaded by noble-metal-free NiS cocatalyst were firstly fabricated by in situ hydrothermal method. The as-synthesized heterostructured photocatalysts were characterized by X-ray diffraction (XRD), transmission electron microscopy (TEM), high-resolution transmission electron microscopy, UV-visible spectroscopy, nitrogen absorption, photoluminescence (PL) spectra, transient photocurrent responses and electrochemical impedance spectroscopy (EIS) measurements. Their photocatalytic activity for hydrogen production was evaluated using an aqueous solution containing triethanolamine under visible light ($\lambda \geqslant 420$ nm). The results clearly demonstrated that the ternary hybridization of NiS cocatalyst, 1D CdS nanorods and 2D g-C_3N_4 nanosheets is a promising strategy to achieve highly efficient visible-light-driven photocatalytic H_2 evolution. Among all the photocatalysts employed, the ternary hybrid g-C_3N_4-CdS-9%NiS composite materials show the best photocatalytic performance with a H_2-production rate of 2563 umol $h^{-1}g^{-1}$, which is 1582 times higherthan that of the pristine g-C_3N_4. The enhanced photocatalytic activity was ascribed to the combined effects of NiS cocatalyst loading and the formation of the intimate nanoheterojunctions between 1D CdS nanorods and 2D g-C_3N_4 nanosheets, which was favorable for promoting charge transfer, improving separation efficiency of photoinduced electron-hole pairs from bulk to interfaces and accelerating the surface H_2-evolutioth kinetics. This work would not only provide a promising photocatalyst candidate for applications in visible-light H_2 generation, but also offer a new insight into the construction of highly efficient and stable g-C_3N_4-based hybrid semiconductor nanocomposites for diverse photocatalytic applications.

1. Introduction

The hydrogen (H_2), as one of the most green and sustainable energy carrier to substitute traditional fossil fuels, has attracted tremendous interest in a number of scientific and technological fields.[1] In the future hydrogen economy, the heterogeneous photocatalytic hydrogen generation form water splitting powered by renewable and sustainable solar energy has been regarded as one of the most eco-friendly strategies for clean hydrogen production.[2-4] Especially, since the Honda–Fujishima effect of water splitting was discovered using a TiO_2 photoelectrode in 1972,[5] enormous efforts have been devoted toward the developments of various H_2-generation photocatalysts.[3, 6] However, so far, this technology is still far from industrial applications on account of its low solar energy conversion and utilization efficiencies, and limited production capacity. Without exaggeration, no one single photocatalyst could satisfy all the requirements for practical water splitting, including suitable band gaps and positions, low costs, high activity and stability.[7, 8] Thus, apart from the development of new photocatalysts, it is increasingly urgent to pay more attention to the resolution of many important scientific issues in the existing H_2-evolution photocatalysts, such as increasing visible-light harvesting, suppressing rapid charge recombination and improving the photostabilities.[3] In recent years, it has been widely recognized that the photocatalysts should be highly functional materials.[2] Generally speaking, there are three typical processes in photocatalytic water splitting, including photon absorption (I), charge separation and migration to surface active sites (II), and surface electrocatalytic reactions (III). [2, 3] Since a lot of visible-light-driven photocatalysts have been available, optimizing both steps (II) and (III) is crucial to achieving highly efficient and stable H_2 evolution.

Among various kinds of semiconductor photocatalysts, noble metal-free polymeric graphite-like carbon nitride (g-C_3N_4) and CdS have proven to be two kinds of promising candidates for visible-light-responsive photocatalytic applications such as H_2 generation,[9-12] dye degradation,[13-16] CO_2 reduction[17-21] and selective organic synthesis[22-24] due to its low costs, easy

preparation, and suitable band gaps and levels. However, the pristine g-C_3N_4 seriously suffer from insufficient poor electrical conductivity, low charge mobility and specific surface area, moderate water oxidation ability, and fast recombination rate of photo-generated electron-hole pairs.[25] Meanwhile, the strong photocorrosion process of well-studied CdS semiconductor generally could lead to sulphur deposition on CdS and Cd^{2+} dissolution, greatly limiting their activity and practical applications.[2] Therefore, a variety of approaches such as loading cocatalysts,[26] constructing heterojunctions with other semiconductors or nanocarbon materials,[27-29] doping metal or nonmetal elements,[25, 30, 31] and forming the mesoporous or nanostructured materials,[32-35] have been developed to improve their photocatalytic efficiency and stability. Among them, forming nano-heterojunctions between g-C_3N_4 and CdS has been widely investigated due to their well-matched band energy alignment, which could not only efficiently enhance the visible-light absorption of g-C_3N_4, but also suppress the photocorrosion of CdS and promote charge separation.[36-38] To date, although CdS quantum dots (or nanoparticles)/bulk g-C_3N_4[37-40] and CdS nanorods (or nanoparticles)/graphene nanosheets[19, 22, 41-44] hybrid photocatalysts have been deeply investigated, there are few reports on the in-situ growth of 1D CdS nanorods on g-C_3N_4 nanosheets in aqueous solutions up to now. Therefore, it is an interesting topic to develop the in-situ growth of CdS nanorods on g-C_3N_4 nanosheets with intimate interface contacts for enhanced photocatalytic H_2 production.

Notably, the famous noble-metal Pt as a H_2-evolution cocatalyst was generally loaded onto the CdS/g-C_3N_4 heterojunctions to further enhance their H_2-generation activity.[36-38] Unfortunately, Pt is too scarce and expensive for the purpose of widespread applications. Thus, it remains a great challenge to develop noble metal-free cocatalysts with a high H_2-evolution activity and a low overpotential to replace Pt.[45-47] To this end, it has been recently demonstrated that the loading of noble metal-free NiS cocatalyst could significantly enhance the H_2-evolution activity of bulk g-C_3N_4,[26, 48, 49] $Zn_xCd_{1-x}S$[50, 51] and CdS,[11, 52] respectively. However, to the best of our knowledge, there have been no available reports about the H_2 generation over noble metal-free NiS cocatalyst modified earth-abuandant CdS nanorods/g-C_3N_4 hterojunctions.

Herein, to synergistically maximize the H_2-evolution activity, we detail a facile hydrothermal route to synthesize ternary hybrid robust photocatalysts by using the combined strategies of froming nanostructures, constructing heterostructured nanocomposites and loading noble metal-free NiS cocatalyst. The earth-abundant CdS nanorods/g-C_3N_4 nanosheets 1D/2D hybrid nanoheterojunctions were constructed through in-situ growth of CdS nanorods on the g-C_3N_4 nanosheets from the Cd-containing carbon nitride (Cd-g-C_3N_4) compounds, which is similar to previous Fe/g-C_3N_4 and Zn/g-C_3N_4 compounds.[53] Moreover, noble-metal-free NiS nanoparticles were also loaded on g-C_3N_4-CdS nanoheterojunctions via precipitating nickel acetate in the presence of a large excess of thiourea under hydrothermal conditions. The possible mechanism for the significant enhancement in photocatalytic activity of the g-C_3N_4-CdS-NiS ternary nanohybrids was also proposed. This work demonstrates that constructing 1D/2D hybrid materials loaded by noble-metal-free cocatalyst is a promising strategy for developing high efficiency earth-abundant photocatalysts for application in photocatalytic H_2 evolution under visible light irradiation.

2. Experimental section

2.1. Materials.

All reagents, including cyanamide (CH_2N_2, 50% in water), cadmium nitrate tetrahydrate ($Cd(NO_3)_2{\cdot}4H_2O$), nickel acetate ($Ni(CH_3COO)_2{\cdot}4H_2O$) and thiocarbamide ($H_2NCSNH_2$), were of analytical grade and used as received without further purification.

2.2. Synthesis

The g-C_3N_4-CdS-NiS ternary nanohybrids and CdS nanorods/g-C_3N_4 nanosheets 1D/2D hybrid nanoheterojunctions were fabricated by a facile two-step wet chemistry approach, as illustrated in Scheme 1. The Cd-g-C_3N_4 was firstly prepared by a simple and efficient electrostatic adsorption method. Then, the ternary or binary nanocomposites were synthesized by a hydrothermal in-situ growth process. The detailed experimental conditions and steps were as follows:

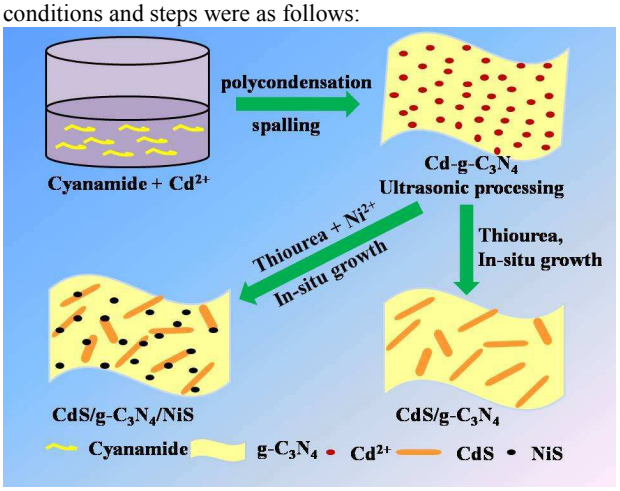

Scheme 1 Schematic diagram of the synthetic route of g-C_3N_4/CdS/NiS ternary nanocomposites.

(I) Synthesis of pristine g-C_3N_4 and Cd-g-C_3N_4

In a typical procedure, 0.3752 g $Cd(NO_3)_2{\cdot}4H_2O$ was dissolved in 10 mL distilled water and then 10 mL cyanamide was added and stirred for 1h. Afterwards the mixture was transferred into a Teflon-lined stainless-steel autoclave and heated at 150 °C for 4 h. The autoclave was cool down naturally and a yellow precipitate was collected, washed, and dried in air. And that, the obtained yellow solid was transferred to a crucible with lid and heated under a nitrogen gas at 2.3 ℃ min^{-1} up to 550 ° C and kept at this temprature for another 4 h.

According to the same method described above, the pristine g-C_3N_4 was prepared in the absence of cadmium nitrate and ultrasonic treatment.

(II)Synthesis of g-C_3N_4 nanosheets/CdS nanorods hybrid materials

In a typical synthesis, 0.3 g obtained Cd/g-C_3N_4 powders were firstly dispersed in a thiourea solution via ultrasonic exfoliation for 2 h. The mixed suspension was transferred into Teflon-lined stainless autoclave and kept at 150 °C for 4 h in an oven before cooling down to room temperature. Finally, the sample was collected, washed with distilled water several times, vacuum-dried and stored for further characterization.

(III)Synthesis of g-C_3N_4/CdS/NiS ternary nanohybrids

The 0.3 g obtained Cd/g-C_3N_4 powders were dispersed in 10 mL of distilled water via ultrasonic treatment for 30 min, and then a calculated amount of 0.05 M nickel acetate solution was added and stirred for 1 h. After that, 10 mL of thiourea solution (2 g thiourea) was dropwise added. The mixed suspension was transferred into Teflon-lined stainless autoclave and kept at 150 °C for 4 h in an oven before cooling down to room temperature. Finally, the sample was collected, washed with distilled water several times, vacuum-dried and stored for further characterization.

2.3. Characterization

The crystal structure of samples was investigated using X-ray diffraction (XRD; Rigaka D/max 2500v/pc X-ray diffractometer) with Cu K α radiation at a scan rate of 4° min^{-1}. The UV-visible absorption was measured by using a UV-vis spectro-photometer (TU1901, China). The X-ray photoelectron spectroscopy (XPS) was performed with a VG ESCALAB250 surface analysis system using a monochromatized Al KαX-ray source (300 W, 5 mA, and 15 kV). The base pressure was about 3 x 10^{-9} mbar. The shift of the binding energy owing to relative surface charging was corrected using the C 1s level at 284.6 eV as an internal standard.The specific surface area was determined by the Brunauer–Emmett–Teller (BET) method at 77 K. Nitrogen adsorption-desorption isotherms were measured on a Quantachrome NOVA1000 Sorptomatic apparatus. Trans-mission electron microscopy (TEM) images and high-resolution transmission electron microscopy (HRTEM) images, and selected area electron diffraction (SAED) patterns were collected on an F20 S-TWIN electron microscope (Tecnai G2,FEI Co.), at a 200 kV accelerating voltage. The photoluminescence (PL) spectra were measured using a LS 50B (Perkin Elmer, Inc., USA) with an excitation wavelength of 363 nm at room temperature.

2.4. Photocatalytic reaction procedures

Photocatalytic water splitting was carried out in a LabSolar H 2photocatalytic hydrogen evolution system (Perfectlight, Beijing) including a 300 W Xe lamp (PLS-SXE300, Beijing Trusttech). In a typical photocatalytic reaction, 50 mg of powder sample was dispersed in an aqueous solution (100 mL) containing 10% triethanolamine by volume. Then the system was sealed and vacuumized to keep the pressure as -0.1 MPa. Afterwards, a circular cooling water system was turned on and the reactor was irradiated with Xe lamp (300 W) with a UV cut-off filter (λ≥420nm) under magnetic stirring. The gases evolved were analyzed on line with a gas chromatograph (GC-7900, TCD, with N_2 as carrier gas) after 0.5 h of illumination. The reaction was continued for 2.5 h.

2.5 Electrochemical tests

The working electrodes were prepared as follows: 5 mg of photocatalyst powder was added into 2 ml of ethanol and 20uL of 0.25% Nafion solution to make a slurry, and the powders were dispersed using ultrasonication. 500uLof the solutionwas injected onto a 2 × 6 cm^2 fluorine-doped tin-oxide (FTO) glass substrate. The resulting electrodes were dried in an oven and calcined at 150□ for 1h in a N_2 gas flow.

2.5.1. Transient photocurrent tests.

Transient photocurrent experiments were conducted on an electrochemical analyzer (BAS100 Instruments) in a standard three-electrode system using the as-prepared working electrodes as the working electrodes, a Pt wire as the counter electrode, and Ag/AgCl (saturated KCl) as a reference electrode. 0.5 M Na_2SO_4 aqueous solution was used as the electrolyte. A Xe lamp (300 W) with a UV cut-off filter (λ≥420nm) was used as a light source.

2.5.2. The electrochemical impedance spectroscopy (EIS)

The electrochemical impedance spectra (EIS) of above-mentioned working electrodes in the three-electrode system were also recorded via a computer controlled IM6e impedance measurement unit (Zahner Elektrik, Germany) over a frequency range of 0.01–10^5 Hz with an ac amplitude of 5 mV, under UV light and in the dark. 0.1 M Na_2S and 0.02 M Na_2SO_3 aqueous solutions was used as the electrolyte.

2.5.3 Electrocatalytic hydrogen evolution

The electrocatalytic hydrogen evolution was tested using a three-electrode cell. Linear sweep voltammetry with a 5 mVs^{-1} scan rate was performed in 0.5 M H_2SO_4 electrolyte solution under continuous purging with N_2. The reference, counter, and working electrodes were a reversible hydrogen electrode (RHE), a Pt flake, and a glassy carbon electrode, respectively. The working electrodes were prepared as follows: 2 mg of photocatalyst powder were ultrasonically dispersed in 1mL ethanol (for > 1 hour) and then deposited on a glassy carbon electrode with 10 uLof the solution. After drying the ink, 25 µl of 5 wt% Nafion was diluted with 1 ml of ethanol; 5 µl of that solution was then added on top of the catalyst layer. Time dependence of the current density obtained for g-C_3N_4/9%NiS at a static potential of -803 mV for 6 h in 0.5m H_2SO_4.

3. Results and Discussion

3.1. X-ray Diffraction (XRD)

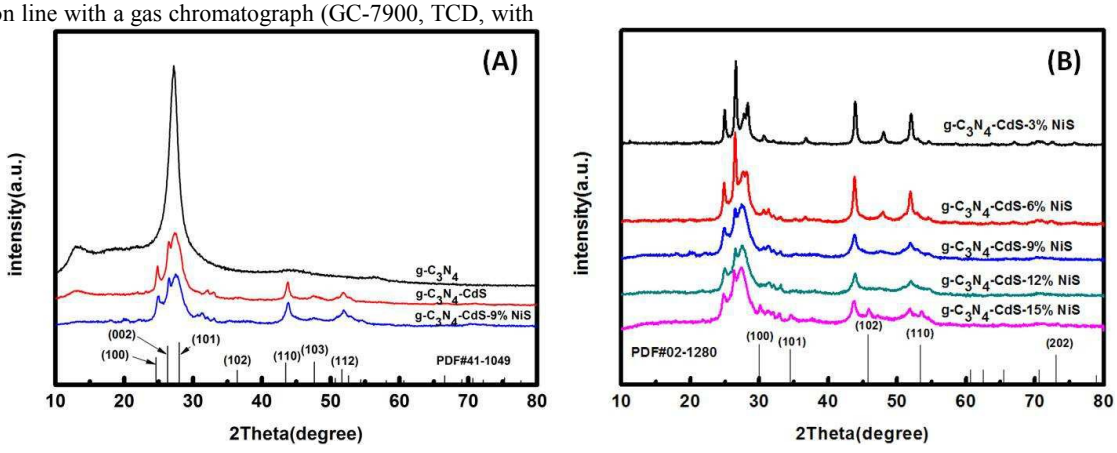

Fig. 1 XRD patterns of the as-prepared composite samples.

The crystalline structure and phase purity of the as-prepared samples was investigated by XRD measurements. The X-ray diffraction patterns of pure g-C_3N_4, g-C_3N_4-CdS and g-C_3N_4-CdS-9% NiS photocatalysts are shown in Fig. 1A. As can be seen from Fig. 1A, two distinct diffraction peaks were observed at approximately 2θ= 27.5° and 13.2° for pure g-C_3N_4 sample, which are also consistent with those of g-C_3N_4 in the literature.[54] The results indicate that these two diffraction peaks can be indexed to the (002) and (100) diffraction planes for g-C_3N_4, respectively (JCPDS # 87-1526).[55, 56] The strong (002) peak at 2θ= 27.5°, corresponding to the interlayer distance of 0.325 nm, is a characteristic interlayer stacking reflection of conjugated aromatic systems, indicating that pure bulk g-C_3N_4 was well crystallized.[54] Interestingly, it was also found that the intensity of this (002) peak in composite photocatalysts significantly decreases, as compared that of bulk g-C_3N_4. The possible reasons can be ascribed to the formation of ultrathin g-C_3N_4 nanosheets through a liquid exfoliation process,[32] and the introduction of CdS nanorods. Furthermore, it was also observed from Fig. 1A that the characteristic peaks with 2θ values of 24.81°, 26.51°, 28.18°, 36.62°, 43.68°, 47.84° and 51.82° were assigned to diffraction peaks from the (100), (002), (101), (102), (110), (103) and(112) crystal planes of CdS (JCPDS#41-1049), respectively.[57] These peaks fully indicate that well-crystallized hexagonal CdS phase with lattice parameters a = 4.14 Å and c = 6.72 Å was successfully loaded on the g-C_3N_4 nanosheets. In addition, the XRD patterns of g-C_3N_4-CdS with different NiS loading percentage are shown in Fig. 1B. As shown in Fig. 1B, the XRD pattern of g-C_3N_4-CdS-15%NiS reveals diffraction peaks at 30.17°, 34.74°, 46.03°, 53.55° and 73.33°, which can attributed to diffraction peaks from the (100),(101),(102),(110) and (202) crystal planes of hexagonal NiS phase (JCPDS#02-1280). However, no diffraction peaks of NiS were observed in the XRD pattern of g-C_3N_4-CdS composites with other NiS loading percentages, which may be due to the low contents and high dispersion of NiS in these samples.

3.2. TEM and EDX characterization

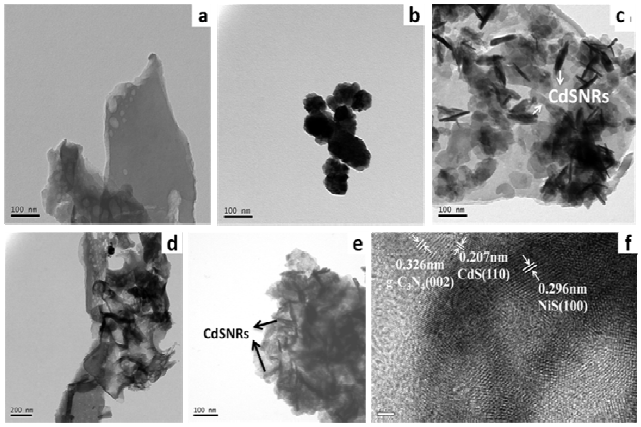

Fig. 2 the as-prepared composite samples:(a) g-C_3N_4; (b) CdS; (c)g-C_3N_4-CdS; (d) g-C_3N_4-9%NiS; (e) g-C_3N_4-CdS-9%NiS;(f) HRTEM images of g-C_3N_4-CdS-9%NiS.

In order to investigate the morphology and microstructure of g-C_3N_4-CdS-NiS composites, TEM images of different samples were carried out. Fig. 2a and 2b show the representative TEM images of the bulk g-C_3N_4 and CdS, respectively. As can be seen in Fig. 2a, the as-prepared bulk g-C_3N_4 is indeed composed of few nanometer sized 2D nanostructures assembled from few-layered ultrathin nanosheets. Also, it can be seen from Fig. 2b that the pure CdS structures were made up of nanoparticles with an average diameter of approximately 60–100 nm. Furthermore, the TEM images of binary systems such as g-C_3N_4-CdS and g-C_3N_4-9%NiS were also investigated, which were shown in Fig. 2c and 2d, respectively. Clearly, it can be observed from Fig. 2c that CdS nanorods were distributed uniformly on the surface of g-C_3N_4 nanosheets, avoiding the irregular aggregation of pure CdS nanorods in the absence of g-C_3N_4 nanosheets. Further observation shows that the length and diameter of CdS nanorods were about 10 and 100 nm, respectively. It is interesting to note that the thickness of g-C_3N_4 of g-C_3N_4-CdS (in Fig. 2c) is much smaller than that of bulk g-C_3N_4 (in Fig. 2a), suggesting the bulk g-C_3N_4 have been only partially exfoliated into 2D g-C_3N_4 nanosheets through 2-h ultrasonic process. However, it is still far from single-layer or few-layer g-C_3N_4 nanosheets, implying that 2-h ultrasonic process is not enough long to obtain completely exfoliated few-layer g-C_3N_4 nanosheets. Thus, to construct more efficient g-C_3N_4 nanosheet-based photocatalysts, a long-time ultrasonic treatment and new exfoliation methods are highly expected in future studies.[58-60] In addition, some irregular NiS nanoparticles with the size of 10−40 nm could be found to be well dispersed on the surface of 2D bulk g-C_3N_4 nanostructures (see Fig. 2d). Compared with Fig. 2b, it is easily indentified from Fig. 2e that some CdS nanorods in the g-C_3N_4-CdS-9%NiS sample were also covered with a strongly adherent NiS layer. To further reveal the intimate interface contacts between different components in the ternary nanohybrids, the HRTEM image of g-C_3N_4-CdS-9%NiS sample was performed, as displayed in Fig. 2f. Obviously, the HRTEM image of the g-C_3N_4-CdS-9%NiS sample exhibits clear lattice fringes of NiS nanoparticles and CdS nanorods on top of those of 2D C_3N_4 nanosheets. It is obvious that the lattice spacing of *ca.* 0.324 nm corresponds to the (002) plane of hexagonal g-C_3N_4 (JCPDS #87-1526). The lattice fringes of with spacing of *ca.* 0.207 and 0.296nm can be assigned to the (110) and (100) plane of hexagonal CdS (JCPDS #41-1049) and NiS (JCPDS #02-1280), respectively. The HRTEM results clearly demonstrated that intimate heterostructures in the ternary nanohybrids have been achieved instead of a simple physical mixture of three components, which are responsible for rapid charge separation in the electron-transfer process and photoactivity enhancement. More importantly, the EDS of g-C_3N_4-CdS-9%NiS sample was shown in Fig. 3, further confirming that the sample contains the obvious signals of C, N, Cd and S elements.

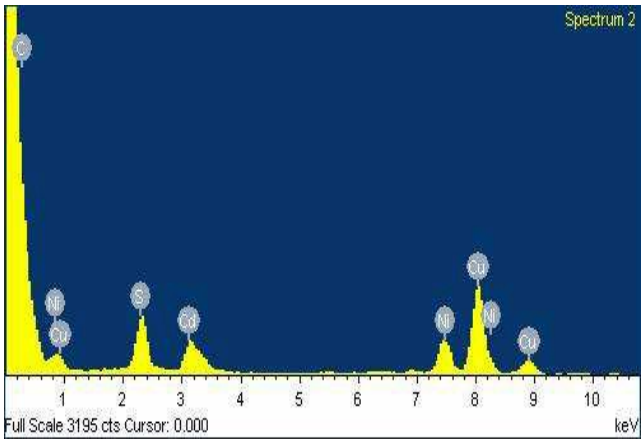

Fig. 3 EDS spectrum of g-C_3N_4-CdS-9%NiS sample.

Based on above results, it is clear that the in-situ growth of CdS nanorods could be mainly achieved using the Cd-containing carbon nitride (Cd-g-C_3N_4) nanosheets as precursors. On the contrary, only CdS nanoparticles could be obtained in the absence of Cd-containing g-C_3N_4 nanosheets. It is known that g-C_3N_4 has a pretty good capacity to capture cations through the strong interactions between the cations and the negatively charged nitrogen atoms within the g-C_3N_4.[9, 61] Therefore, it is proposed that the possible in-situ growth of CdS nanorods along the incorporated Cd^{2+} ions into the framework of g-C_3N_4 could proceed in the void zones around the "nitrogen pots".[61]

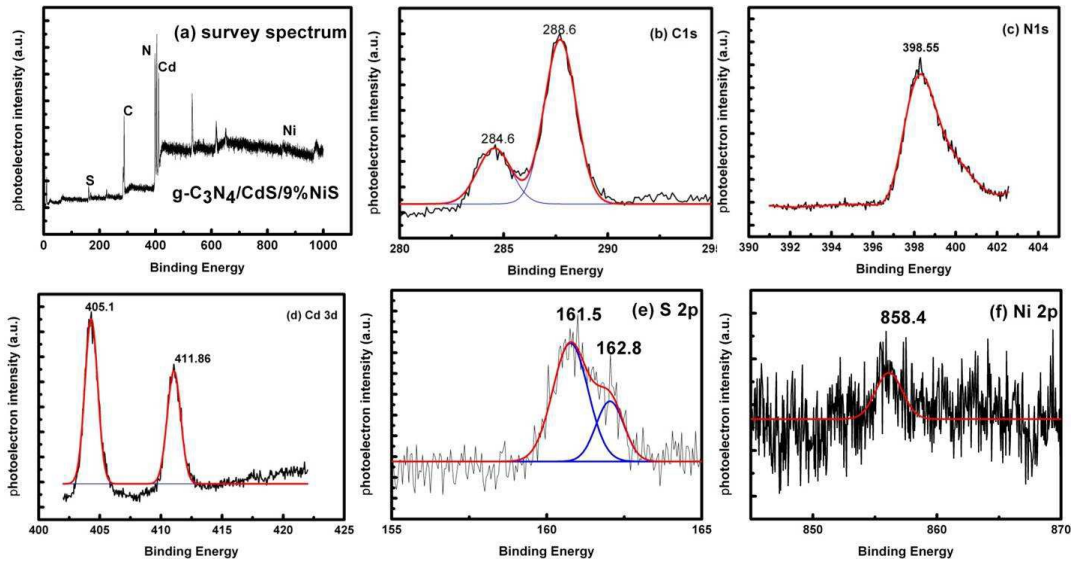

Fig. 4 XPS spectra of g-C_3N_4-CdS-9%NiS; survey spectrum (a) C_{1s} (b) N_{1s} (c) Cd_{3d} (d) S_{2p} (e) Ni_{2p} (f).

The XPS measurements are employed to further confirm the chemical composition and surface chemical state of the as-prepared g-C_3N_4-CdS-9%NiS, as depicted in Fig. 4a-f. The typical XPS survey spectrum of the g-C_3N_4-CdS-9%NiS sample is displayed in Fig. 4a, which undoubtedly indicates the co-existence of the elements C, N, Cd, Ni, S and a small amount of O. The corresponding high resolution XPS spectra of C 1s, N 1s, Cd 3d, S2p and Ni2p of the g-C_3N_4-CdS-9%NiS sample are shown in Fig. 4b–f, respectively. Obviously, the high-resolution spectrum of C 1s shown in Fig. 4b could be fitted into two peaks centered at 284.6 eV and 288.6 eV. The peak at 284.6 eV could be indexed to the sp^2 C–C bonds in a purely carbonaceous environment,[19] which may originate from the graphitic or amorphous carbon species adsorbed on the surface of the g-C_3N_4-CdS-9%NiS sample due to its exposure to air.[37] Whereas, the main peak located at 288.6 eV could be attributed to the sp^2-bonded carbon in the triazine rings (N–C=N), confirming the major carbon environment in the g-C_3N_4.[38] It is also observed from Fig. 4c that the main peak of N 1s spectrum located at 398.55 eV obviously exhibits an asymmetrical feature, which is commonly associated with the sp^2-bonded N in N-containing aromatic rings (N–C=N) in g-C_3N_4, further indicating the presence of g-C_3N_4.[37, 38] In addition, the binding energies of Cd 3d (Fig. 43d) are determined to be 405.1 eV and 411.86 eV (Fig. 4d), which match well with the reported values of the Cd $3d_{5/2}$ and Cd $3d_{3/2}$ for Cd^{2+} in the CdS nanorods.[57] Fig. 4e shows the main S 2p peaks centered at 161.5 eV and 162.8 eV, which are in good accordance with the literature values for the binding energies of sulfide ions in CdS nanorods and NiS cocatalysts.[26, 62] The high-resolution XPS spectra of Ni 2p in Fig. 4f exhibits one

weak peak corresponding to the binding energies of 858.4 eV, which are close to the reported values for NiS.[26, 48] In addition, the weight concentrations of CdS and NiS were measured to be about 6.3% and 8.8%, which are very close to their corresponding design values. The above results further confirmed that the as-obtained g-C_3N_4-CdS-9%NiS sample is composed of g-C_3N_4, CdS and NiS.

3.3. Textural properties and UV-visible absorption spectra

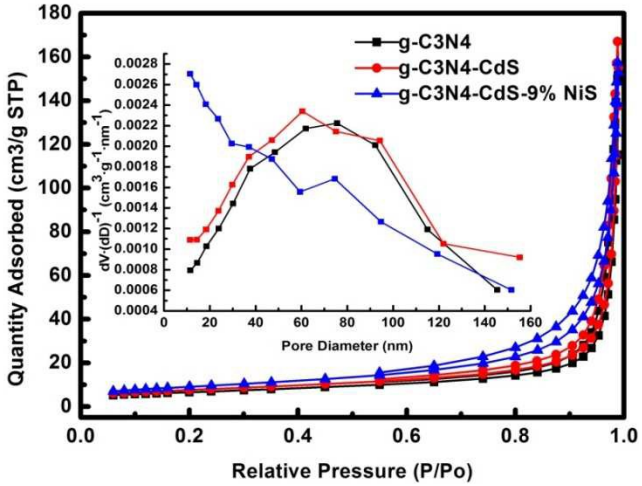

Fig. 5 Nitrogen adsorption-desorption isotherms and the corresponding pore-size distribution curves (inset) of g-C_3N_4, g-C_3N_4-CdS and g-C_3N_4-CdS-9%NiS

Table 1 Porous structure parameters of g-C_3N_4, g-C_3N_4-CdS and g-C_3N_4-CdS-9%NiS samples

Photocatalysts	BET surface area (m^2g^{-1})	specific pore diameter (nm)	Mean pore volume (cm^3g^{-1})
g-C_3N_4	23.1109	42.8392	0.235496
g-C_3N_4-CdS	26.7301	38.6397	0.239828
g-C_3N_4-CdS-9%NiS	32.4818	28.0720	0.237706

The textural properties of the prepared samples were analyzed by nitrogen adsorption-desorption experiments. Fig. 5 shows the adsorption-desorption isotherms of nitrogen at 77 K and the corresponding pore size distributions (the inset) for g-C_3N_4, g-C_3N_4-CdS and g-C_3N_4-CdS-9%NiS, respectively. As shown in Fig. 5, three tested samples show a typical type IV adsorption-desorption isotherm according to the IUPAC classification.[63] Furthermore, obvious H3 hysteresis loops were observed for three samples at high relative pressures close to unity, indicating the formation of the slit-shaped mesopores and macropores due to the aggregates of plate-like g-C_3N_4 nanosheets.[63] The pore-size distributions (inset in Fig. 5) of g-C_3N_4, g-C_3N_4-CdS and g-C_3N_4-CdS-9%NiS composites further confirm the existence of mesopores and macropores. The porous structure parameters of pure g-C_3N_4, g-C_3N_4-CdS and g-C_3N_4-CdS-9%NiS composites are list in Table 1. As listed in Table 1,the BET specific surface area (S_{BET}) of g-C_3N_4, g-C_3N_4-CdS and g-C_3N_4-CdS-9%NiS are 23.11, 26.73 and 32.48 for g-C_3N_4, g-C_3N_4-CdS and g-C_3N_4-CdS-9%NiS, respectively. Clearly, the introduction of CdS nanorods and NiS nanoparticles could lead to the increase of specific surface area and the decrease of pore diameter, implying they have been successfully loaded into the pores of g-C_3N_4 nanosheets. In addition, the significant enhancement in the S_{BET} after loading CdS and NiS may be also beneficial for increasing surface active sites and photoactivities.

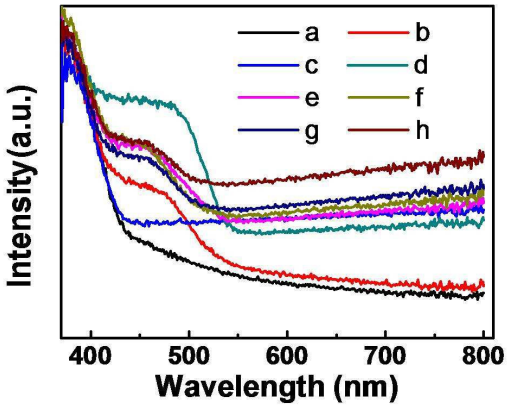

Fig. 6 UV-vis absorption spectra of the as-prepared samples: (a) g-C_3N_4; (b) g-C_3N_4-CdS; (c) g-C_3N_4-9%NiS; (d) g-C_3N_4-CdS-3%NiS; (e) g-C_3N_4-CdS-6%NiS; (f) g-C_3N_4-CdS-9%NiS; (g) g-C_3N_4-CdS-12%NiS; (h) g-C_3N_4-CdS-15%NiS.

The optical properties of pure g-C_3N_4 and its composites were also determined by the UV -Vis diffuse reflectance spectra. Fig.6 depicts the UV-vis absorption spectra of the as-prepared samples. As shown in Fig. 6, the onset of the absorption edge of pure g-C_3N_4 is located at about 450 nm, corresponding to a band-gap energy of 2.75 eV, which is in good accordance with the reported value in the literature.[54] As compared to the pure g-C_3N_4 sample, the composites containing CdS showed a red-shifted absorption edge at around 520 nm, indicating that CdS plays an important role in enhancing the visible-light absorption of g-C_3N_4 as an excellent photosensitizer. The corresponding band-gap energy is estimated to be 2.4 eV, which is consistent with the intrinsic band gap of CdS,[64] further suggesting that CdS nanorods have been successfully introduced into these two composites. Especially for the ternary g-C_3N_4-CdS-NiS nanohybrids and the binary g-C_3N_4-9%NiS, the substantially enhanced light absorption was apparently observed in the visible region ranging from 550 to 800 nm, as compared to pure g-C_3N_4 and g-C_3N_4-CdS samples. Importantly, the visible-light absorption level from 550 to 800 nm also substantially increased with increasing the loading content of NiS co-catalyst. Clearly, the obtained ternary g-C_3N_4-CdS-NiS samples exhibited the strongest absorption intensity in the visible region, which was further confirmed by their observed obvious color change from yellow to green. Thus, this significantly enhanced visible-light absorption can be attributed to the loading of NiS co-catalysts, suggesting that Ni^{2+} ions were highly dispersed on the surface of g-C_3N_4-CdS rather than doped into the CdS lattice. The decreased band gap and enhanced visible-light absorption of the composite samples could lead to efficiently increase the production of photo-generated charges, thus facilitating to the enhancement of their photocatalytic activity.

3.4. Photocatalytic hydrogen production

Cite this: DOI: 10.1039/c0xx00000x

www.rsc.org/xxxxxx

ARTICLE TYPE

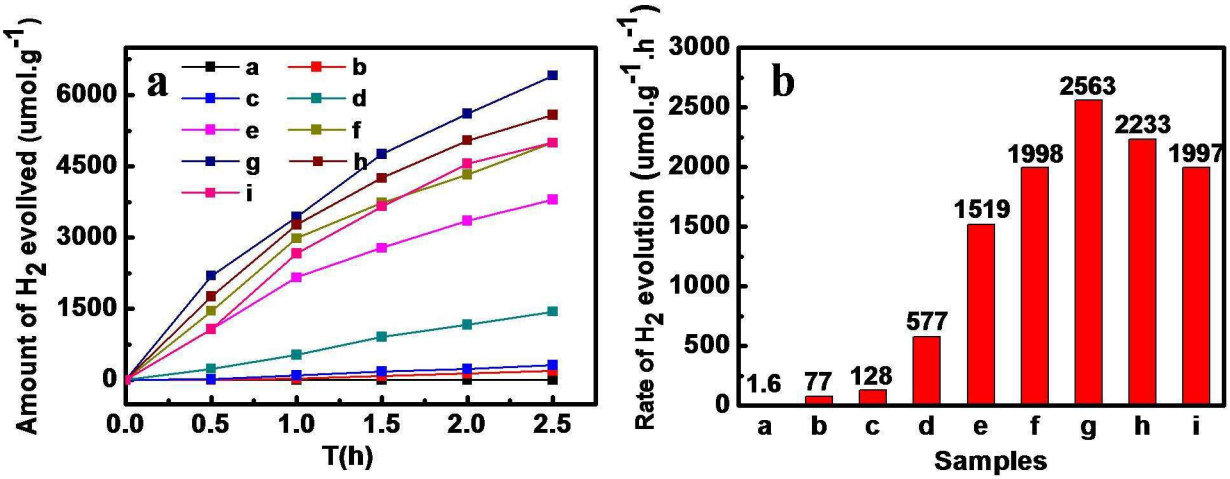

Fig. 7 (A) The average rate of H_2 evolution and (B) Time courses of photocatalytic H_2 evolution over the photocatalysts: (a) g-C_3N_4; (b) g-C_3N_4-CdS; (c) g-C_3N_4 -9%NiS; (d) CdS-9%NiS; (e) g-C_3N_4-CdS-3%NiS; (f) g-C_3N_4-CdS-6%NiS; (g)g-C_3N_4-CdS-9%NiS; (h)g-C_3N_4-CdS-12%NiS; (i) g-C_3N_4-CdS-15%NiS. Reaction conditions: catalyst, 0.05 g; 10 mL triethanolamine;90 mL distilled water; light source, xenon lamp (300 W) with a UV cut-off filter (λ≥420 nm).

To further verify the photocatalytic H_2 generation from water splitting, the H_2-evolution activities of all samples were also examined in aqueous solution containing triethanolamine (10 vol%) as the sacrificial agent under visible light irradiation. No obvious H_2 was detected over all samples in the blank experiments, suggesting that the H_2 was truly generated in the photocatalytic process.[2] Several typical time courses of H_2 evolution from different photocatalysts under visible light irradiation are shown in Fig. 7A. As observed in 7A, the rates of hydrogen evolution over all samples exhibited a non-linear increase during the whole photocatalytic reactions. Obviously, H_2-evolution rate slightly decreased with increasing the time of photocatalytic reaction, implying that photocatalysts are not very stable under light illumination.

For comparison, the average photocatalytic H_2-evolution rates over various photocatalysts with different loading amounts of NiS cocatalysts are also calculated and shown in Fig. 7B. As shown in Fig. 7B, during the 2.5-h photocatalytic reaction process, the average rates of hydrogen evolution were determined to be 1.62, 77, 128,577,1519, 1998, 2563, 2233 and 1997 $\mu mol \cdot g^{-1} \cdot h^{-1}$ for g-C_3N_4, g-C_3N_4-CdS, g-C_3N_4-9%NiS, CdS-9%NiS, g-C_3N_4-CdS-3%NiS, g-C_3N_4-CdS-6%NiS, g-C_3N_4-CdS-9%NiS, g-C_3N_4-CdS-12%NiS and g-C_3N_4-CdS-15%NiS, respectively. Obviously, all of five ternary composite photocatalysts exhibit better photoactivities than the pure g-C_3N_4, binary g-C_3N_4-CdS 2D/1D hybrid photocatalyst, g-C_3N_4-9%NiS and CdS-9%NiS. Especially, the loading of 9%NiS onto the g-C_3N_4-CdS 2D/1D hybrid photocatalyst could achieve the highest H2-evolution rate, which is approximately 33-fold higher than that of sample without loading NiS. Similarly, the average H_2-evolution rate of the g-C_3N_4-CdS 2D/1D hybrid photocatalyst is about 47 times larger than that of the pure g-C_3N_4. As a result, the average H_2-evolution rate of the g-C_3N_4-CdS-9%NiS was about 1582 times that of the pure g-C_3N_4. Moreover, the H_2-evolution activities of g-C_3N_4-CdS-NiS ternary nanohybrids are much higher than those of CdS quantum dots (or nanoparticles)/g-C_3N_4,[37] NiS/g-C_3N_4,[26, 48] MoS_2/g-C_3N_4,[56] Graphene/C_3N_4,[28] WS_2/g-C_3N_4[65] and $Ni(OH)_2$/g-C_3N_4[66] composites. In addition, it should be noted that the H_2 production rate increased firstly and then decreased with further noble metal-free NiS loading. The most probable cause is that appropriate amounts of NiS can act as co-catalysts to suppress the recombination of photoelectrons and holes, thus leading to an enhanced photocatlytic activity for water decomposition over g-C_3N_4-CdS photocatalyst. While, adding an excess amount of NiS (>9%) was shown to reduce the photocatalytic activity of the g-C_3N_4-CdS-NiS ternary nanohybrids, due to the optical shielding effect of NiS cocatalyst and weakened interfacial coupling between C_3N_4 and CdS. From these results, it can be concluded that the synergistic effects of NiS cocatalyst loading and 1D/2D nanoheterojunctions are crucial to achieve the remarkable photoactivity enhancement of the g-C_3N_4-CdS-NiS ternary hybrids.

The photostability of a given photocatalyst is also crucial for its practical application. Thus, the long-term photostability and reproducibility of the as-prepared ternary g-C_3N_4-CdS-9%NiS photocatalyst for H_2 evolution were further evaluated through five consecutive runs under the same conditions. Each cycle was performed under visible light irritation for 2.5 h. After each run, the reaction system was re-evacuated. Fig. 8 displays the recycling measurements of photocatalytic H_2 evolution over g-C_3N_4-CdS-9%NiS sample under visible light irradiation (λ≥420 nm). As seen in Fig. 8, there

is a noticeable activity loss (almost 20%) in the second recycle. It is believed that the decreased catalytic activity over the g-C_3N_4-CdS-9%NiS sample mainly originated from the photocorrosion of some exposed CdS nanorods.[67] Similar trend has been also observed in some published papers.[67, 68] Furthermore, it should be also noted that the H_2 generation rate remains constant after the second recycle, suggesting the ternary hybrid strategy could partially suppress the photocorrosion of CdS in the composite photocatalyst, thus favoring its application in sustainable reuse.

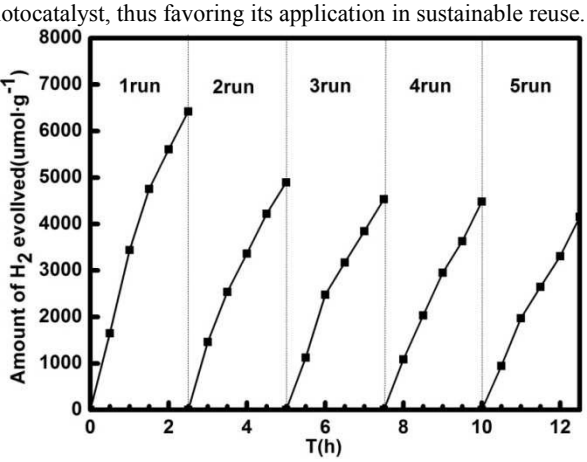

Fig. 8 Repeated time courses of photocatalytic H_2 evolution on g-C_3N_4-CdS-9%NiS sample. Reaction conditions: catalyst, 0.05 g; 10 mL triethanolamine;90 mL distilled water; light source, xenon lamp (300 W) with a UV cut-off filter (λ≥420 nm)

3.5. Discussion of mechanism

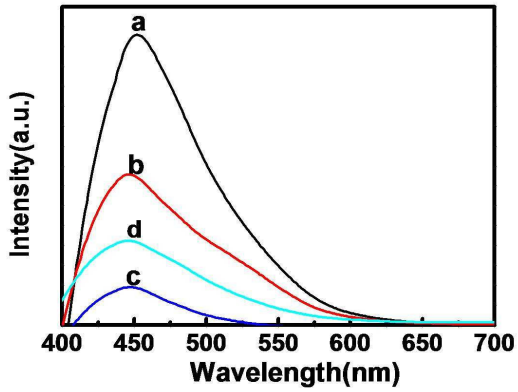

Fig. 9 PL spectra of pure g-C3N4, as well as of the composite photocatalysts at an excitation wavelength of 363 nm: (a) g-C_3N_4; (b) g-C_3N_4-CdS; (c) g-C_3N_4-9%NiS; (d) g-C_3N_4-CdS-9%NiS.

The charge recombination and transfer can be further investigated by photoluminescence (PL) spectra. The PL spectra has been regarded as an efficient approach to study the separation efficiency of the photogenerated electron–hole pairs on the semiconductor upon irradiation. Fig. 9 presents PL spectra of pure g-C3N4, g-C_3N_4-CdS, g-C_3N_4-9%NiS and g-C_3N_4-CdS-9%NiS samples at room temperature with an excitation wavelength of 363 nm. As observed from Fig. 9, it is evident that the pure g-C_3N_4, g-C_3N_4-CdS, g-C_3N_4-9%NiS and g-C_3N_4-CdS-9%NiS exhibit similar emission trends, with the principle peak around 450 nm, which can be attributed to the recombination of electron-hole pairs in the g-C_3N4[69]. The g-C_3N_4-CdS-9%NiS sample was found to have a lower PL intensity than g-C_3N_4-CdS which showed the weaker intensity compare with the pure g-C_3N_4. This indicates that a lower recombination rate of the photoinduced electron–hole pairs can be efficiently realized under visible-light illumination due to the loading CdS and NiS, further leading to significantly enhancing photocatalysis efficiency of the as-prepared g-C_3N_4-CdS-9%NiS sample. However, the g-C_3N_4-9%NiS exhibit a lower PL peak as compared to the g-C_3N_4-CdS-9%NiS sample, indicating the slower charge recombination in the g-C_3N_4-9%NiS. It is believed that the g-C_3N_4-9%NiS sample posses much fewer photo-generated electron-hole pairs, thus leading to the lower charge recombination. As above discuss, the g-C_3N_4-CdS-9%NiS sample exhibits the highest photocatalytic activity. Thus, it is clear that the PL spectra results are in agreement with the photocatalytic activities of corresponding samples in most cases, suggesting the separation efficiency of photoexcited charge carriers plays a significant role in determining the photocatalytic performance of photocatalysts.

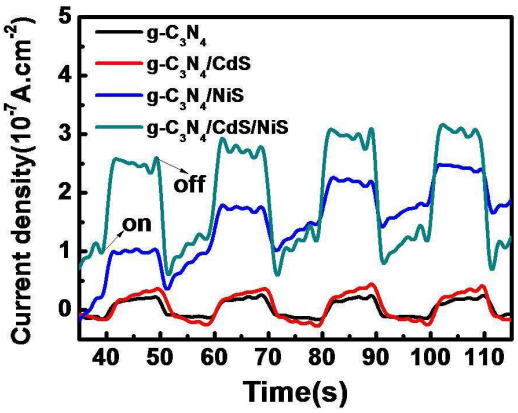

Fig. 10 Transient photocurrent responses (*I–t* curves) of different photocatalysts in 1 M Na_2SO_4 aqueous solution under visible light irradiation at 0.5 V vs Ag/AgCl.

To further deeply understand the photocatalytic enhancement mechanism for H_2 evolution, the transfer and separation of photo-generated charge carriers were also investigated through the photoelectrochemical (PEC) analysis. The transient photocurrent - time (I–t) curves recorded for the above three samples under intermittent visible light irradiation (λ>420 nm) were demonstrated in Fig. 10A. As observed in Fig. 10A, it is obvious that the g-C_3N_4-CdS-9%NiS photocatalysts exhibit apparently boosted photocurrent density as compared to unmodified g-C_3N_4 and binary samples, respectively. Notably, the photocurrent of g-C_3N_4-9%NiS sample is much higher than that of the g-C_3N_4-CdS, indicating that the NiS co-catalysts could more efficiently enhance the interfacial charge transfer. These PEC results suggest that the ternary hybrids could achieved remarkably improved

separation and transfer of photo-excited electron–hole pairs, thus greatly contributing to the photoactivity enhancements.

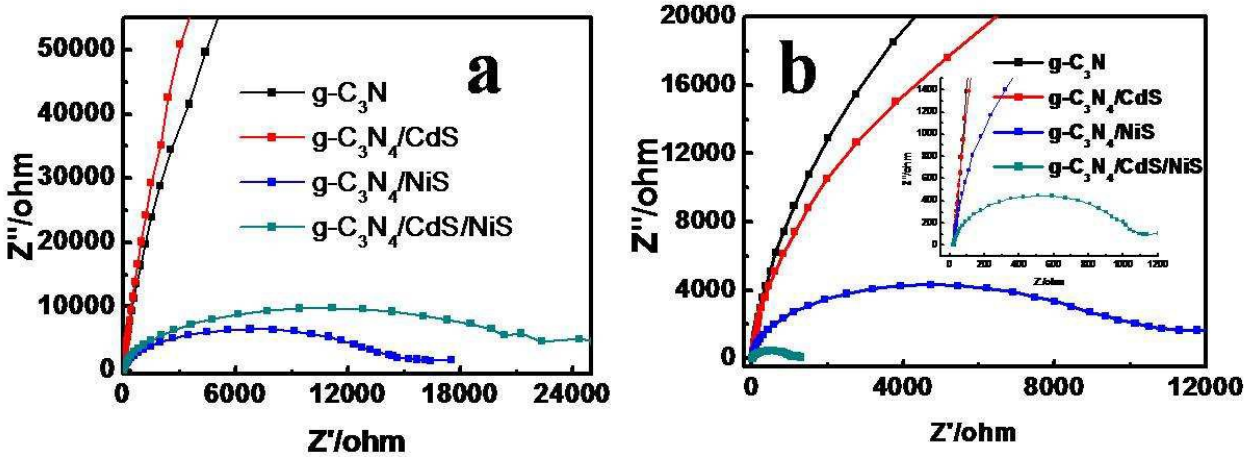

Fig. 11 Nyquist plots of different electrodes in 0.5m H_2SO_4, (a) in the dark; (b) under visible light illumination.

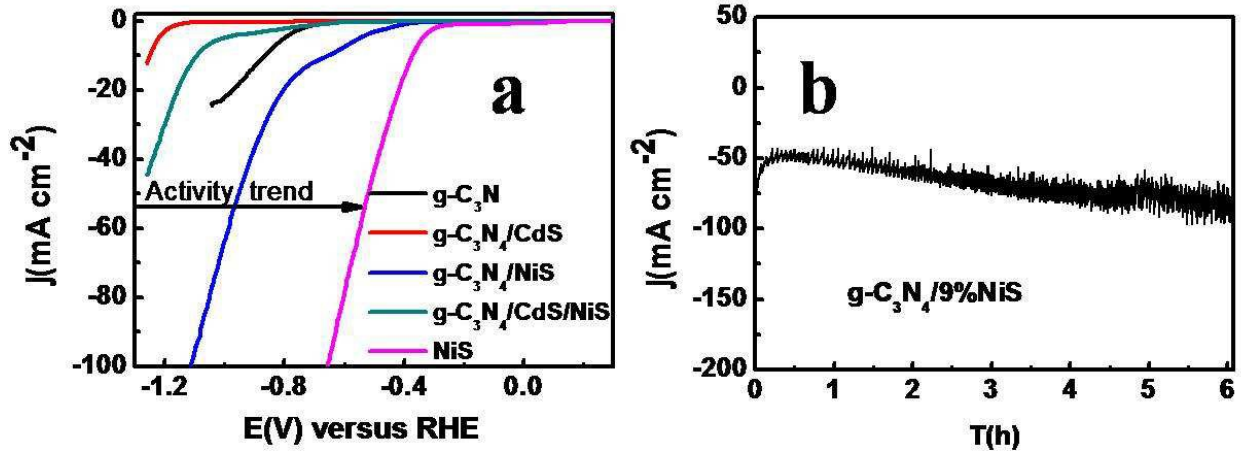

Fig. 12 (a) Polarization curves of different samples were measured at a scan rate of 50 mVS^{-1} in 0.5 M H_2SO_4 acidic solution; (b) Time dependence of the current density obtained for g-C_3N_4-CdS-9%NiS at a static potential of -803 mV for 6 h in 0.5 M H_2SO_4.

To further confirm the enhanced charge separation rate, the electrochemical impedance spectra (EIS) in the dark and under visible light were also performed, which is one of the most powerful techniques to study the interfacial charge transfer and recombination rates occurring in the three-electrode systems. The EIS Nyquist plots of four different samples are shown in Fig. 11. As displayed in Fig. 11, the g-C_3N_4-CdS-9%NiS photocatalyst exhibits the smallest semicircle in the middle-frequency region in comparison with the g-C_3N_4, g-C_3N_4-CdS and g-C_3N_4- 9%NiS, which indicates the fastest interfacial electron transfer in the g-C_3N_4-CdS-9%NiS sample. It is believed that the combined effects, including the loading of NiS co-catalysts and stronger interfacial interaction between CdS and g-C_3N_4, lead to the accelerated charge transport and separation, thus resulting in the significantly improved photocatalytic H_2-production activity. Comparing the electrochemical impedance spectra (EIS) in the dark and under visible light irradiation, it is clearly observed that the loading of NiS nanoparticles is favorable for the charge separation in each case, indicating the positive roles of loaded NiS nanoparticles as H_2-evolution electrocatalysts or co-catalysts. However, CdS can only accelerate the charge separation in binary or ternary samples under visible-light illumination, further confirming the important roles of CdS as an excellent photosensitizer in boosting the photocatalytic activities.

It is generally accepted that the H_2-evolution reactions caused by photo-generated electrons on the surface active sites are similar to those in electrolysis.[2] To further indentify the positive roles of NiS co-catalysts in this system as active sites, the

polarization curves and the time dependence of current density were also carried out. Fig. 12a shows the electrocatalytic H_2-evolution activity for typical five kinds of nanomaterials using a standard three-electrode configuration in 0.5 M H_2SO_4 acidic solution. As observed from these curves in Fig. 12a, among all samples, NiS exhibits the highest catalytic activity for H_2 evolution, while there is no obvious H_2-evolution activity for the g-C_3N_4-CdS sample. It can be also found that the onset potential of NiS for electrocatalytic H_2 evolution is about -0.35 V (in 0.5 M H_2SO_4). According to the linear pH dependence with a slope of 0.059 V per pH, an overpotential of -0.75 V (at pH=7) was obtained, which was obvious lower than those conduction band potentials of CdS (-0.9 V at pH=7) and g-C_3N_4 (-1.25 V at pH=7), respectively.[3, 70] Therefore, the photo-generated electrons from CdS or g-C_3N_4 have enough capacity to enable to drive the electrocatalytic hydrogen evolution over NiS co-catalysts. These results clearly suggested that NiS nanoparticles played a key role in acting as H_2-evolution co-catalysts. In addition, it should be also noted from Fig. 12a that the g-C_3N_4 sample as a metal-free electrocatalyst also exhibits obvious H_2-evolution activity, with an onset potential of -0.75 V (in 0.5 M H_2SO_4), which is consistent with the previous results from Qiao's group.[71-74] Importantly, the elctrocatalytic H_2-evolution activity of g-C_3N_4 could greatly enhanced through loading 9% NiS nanoparticles. Furthermore, as shown in Fig. 12b, the smaller loss in current density also indicates the excellent electrochemical stability of the g-C_3N_4/9%NiS sample. These results further confirmed that the binary g-C_3N_4/NiS material could act as potential bifounctional catalysts for both photocatalytic and electrocatalytic H_2-evolution reaction.

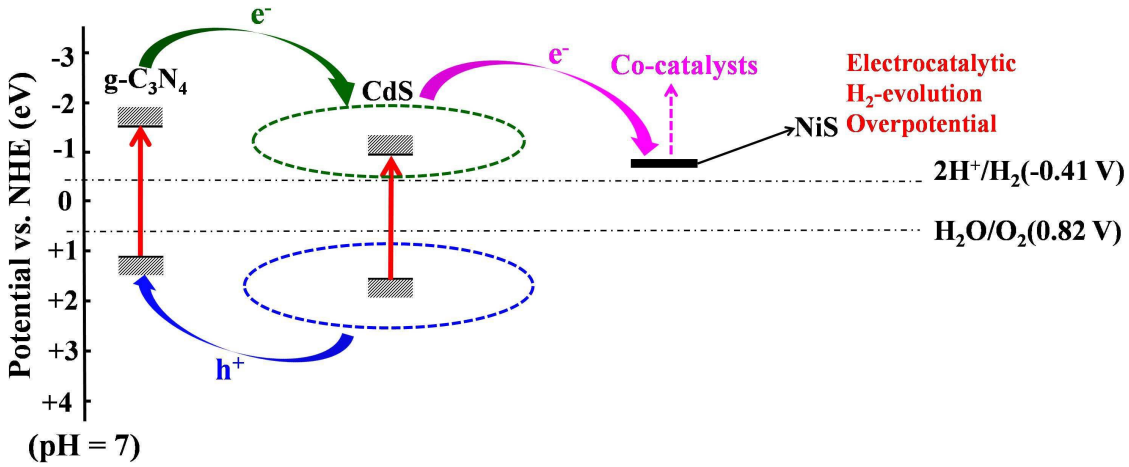

Scheme 2 The schematic diagram of photocatalytic hydrogen evolution over g-C_3N_4-CdS-NiS ternary composite photocatalysts under visible light irradiation.

On the basis of the above results including PL spectra, photocurrent measurements, EIS, and photocatalytic activity results, a probable possible photocatalytic H_2-evolution mechanism using the composite photocatalysts was proposed and illustrated in Scheme 2. Under visible-light irradiation, g-C_3N_4 and CdS was excited and generated electron−hole pairs. The photoinduced electrons on the CB of g-C_3N_4 can directly shift to the CB of CdS, because the conduction band (CB) position of g-C_3N_4 is higher than that of CdS. The electrons excited from the CB of CdS together with the rest electrons on the CB of g-C_3N_4 will accumulate on the NiS and then electrochemically releases H_2 with the reduction of H^+.[48, 52] On the other hand, compared with the CdS quantum dots (or nanoparticles)/g-C_3N_4 photocatalysts, the in-situ growth of 1D CdS nanorods on 2D g-C_3N_4 nanosheets could not only increase the interfacial contact area between CdS and g-C_3N_4, but also enhance the intimacy of their interfacial contacts.[75] These two factors are also favorable for the efficient charge separation, thus facililating the photocatalytic activity enhancement. In a word, the unexpectedly high activity of the g-C_3N_4-CdS-NiS ternary hybrids can be ascribed to the synergistic effects of improved water reduction kinetics through loading NiS cocatalyst and prolonged lifetime of photogenerated electron–hole pairs by constructing 1D/2D nanoheterojunctions. The result demonstrated that loading an appropriate amount of NiS onto the CdS/g-C_3N_4 1D/2D nanohybrids is a promising strategy to develop highly efficient H_2-evolution photocatalysts.

4. Conclusions

In summary, we have successfully demonstrated that g-C_3N_4-CdS-NiS ternary composite photocatalysts can be fabricated by a two-step wet chemistry method. The ternary composite exhibited higher photocatalytic activity for hydrogen evolution than the pure g-C_3N_4 and binary composite photocatalysts. In particular, the g-C_3N_4-CdS-9%NiS shows a 1582-fold increase in the average rate of hydrogen evolution as compared to the g-C_3N_4. The roles of CdS and NiS co-catalysts in boosting the H_2-evolution activity of g-C_3N_4 were revealed. It is believed that the synergistic effects of loading NiS cocatalyst and constructing

CdS/g-C_3N_4 1D/2D nanoheterojunctions can improve the separation of electron–hole pairs, visible-light absorption and water reduction kinetics, thereby achieving an unexpectedly enhanced H_2-evolution activity of the g-C_3N_4-CdS-NiS ternary hybrids. This work could not only provide an excellent candidate for visible-light H_2 evolution, but also offer a new and facile in-situ growth approach to explore highly efficient g-C_3N_4-based hybrid semiconductor nanocomposites for photocatalytic H_2-evolution. The combined strategies deserve more attention in constructing high-activity composite photocatalysts. It is expected that more efficient g-C_3N_4-based composite photocatalysts based on multidimensional hybrid and co-catalyst loading could be achieved for various applications in near future.

5. Acknowledgements

The work was supported by the National Natural Science Foundation of China (20906034, 20963002, 21173088, 21207041 and 21475047). Special thanks to Prof. Can Li in State Key Laboratory of Catalysis, Dalian Institute of Chemical Physics, Chinese Academy of Sciences. This work also partly supported by the State Key Laboratory of Catalysis cooperation project (N-08-08) and the State Key Laboratory of Advanced Technology for Material Synthesis and Processing (2015-KF-7).

Notes and references

College of Materials and Energy, South China Agricultural University, Guangzhou 510642, China. E-mail: Xinliscau@yahoo.com (X. Li), ypfang@scau.edu.cn (Y. Fang), wlscau@163.com (W. Liu)

†Electronic Supplementary Information (ESI) available: [details of any supplementary information available should be included here]. See DOI: 10.1039/b000000x/

‡ Footnotes should appear here. These might include comments relevant to but not central to the matter under discussion, limited experimental and spectral data, and crystallographic data.

1. J. A. Turner, *Science*, 2004, **305**, 972-974.
2. A. Kudo and Y. Miseki, *Chem. Soc. Rev.*, 2009, **38**, 253-278.
3. X. Chen, S. Shen, L. Guo and S. S. Mao, *Chem. Rev.*, 2010, **110**, 6503-6570.
4. K. Maeda and K. Domen, *J. Phys. Chem. C*, 2007, **111**, 7851-7861.
5. A. Fujishima and K. Honda, *Nature*, 1972, **238**, 37-38.
6. Y. Ma, X. Wang, Y. Jia, X. Chen, H. Han and C. Li, *Chem. Rev.*, 2014, **114**, 9987-10043.
7. A. Bard and M. Fox, *Accounts. Chem. Res.*, 1995, **28**, 141-145.
8. A. J. Bard, *J. Am. Chem. Soc.*, 2010, **132**, 7559-7567.
9. S. Cao, J. Low, J. Yu and M. Jaroniec, *Adv. Mater.*, 2015, **27**, 2150-2176.
10. S. Cao and J. Yu, *J. Phys. Chem. Lett.*, 2014, **5**, 2101-2107.
11. J. Zhang, S. Z. Qiao, L. Qi and J. Yu, *Phys. Chem. Chem. Phys.*, 2013, **15**, 12088-12094.
12. Q. Xiang, B. Cheng and J. Yu, *Appl. Catal. B-Environ.*, 2013, **138**, 299-303.
13. M. Zhang, X. Bai, D. Liu, J. Wang and Y. Zhu, *Appl. Catal. B-Environ.*, 2015, **164**, 77-81.
14. M. Zhang, J. Xu, R. Zong and Y. Zhu, *Appl. Catal. B-Environ.*, 2014, **147**, 229-235.
15. X. Bai, L. Wang, R. Zong and Y. Zhu, *J. Phys. Chem. C*, 2013, **117**, 9952-9961.
16. X. Li, T. Xia, C. Xu, J. Murowchick and X. Chen, *Catal. Today*, 2014, **225**, 64-73.
17. X. Li, H. Liu, D. Luo, J. Li, Y. Huang, H. Li, Y. Fang, Y. Xu and L. Zhu, *Chem. Eng. J.*, 2012, **180**, 151-158.
18. X. Li, J. Chen, H. Li, J. Li, Y. Xu, Y. Liu and J. Zhou, *J. Nat. Gas. Chem.*, 2011, **20**, 413-417.
19. J. Yu, J. Jin, B. Cheng and M. Jaroniec, *J. Mater. Chem. A*, 2014, **2**, 3407-3416.
20. J. Yu, K. Wang, W. Xiao and B. Cheng, *Phys. Chem. Chem. Phys.*, 2014, **16**, 11492-11501.
21. K. Wang, Q. Li, B. Liu, B. Cheng, W. Ho and J. Yu, *Applied Catalysis B: Environmental*, 2015, **176–177**, 44-52.
22. N. Zhang, M.-Q. Yang, Z.-R. Tang and Y.-J. Xu, *J. Catal.*, 2013, **303**, 60-69.
23. C. Han, M.-Q. Yang, N. Zhang and Y.-J. Xu, *J. Mater. Chem. A*, 2014, DOI: 10.1039/C4TA04151H.
24. S. Liu, B. Weng, Z.-R. Tang and Y.-J. Xu, *Nanoscale*, 2015, **7**, 861-866.
25. J. Zhang, J. Sun, K. Maeda, K. Domen, P. Liu, M. Antonietti, X. Fu and X. Wang, *Energy Environ. Sci.*, 2011, **4**, 675-678.
26. Z. Chen, P. Sun, B. Fan, Z. Zhang and X. Fang, *J. Phys. Chem. C*, 2014, **118**, 7801-7807.
27. Z. Zhao, Y. Sun and F. Dong, *Nanoscale*, 2014, **7**, 15-37.
28. Q. Xiang, J. Yu and M. Jaroniec, *J. Phys. Chem. C*, 2011, **115**, 7355-7363.
29. L. Ge and C. Han, *Appl. Catal. B-Environ.*, 2012, **117–118**, 268-274.
30. Y. Zhang, T. Mori, J. Ye and M. Antonietti, *J. Am. Chem. Soc.*, 2010, **132**, 6294-6295.
31. G. Zhang, M. Zhang, X. Ye, X. Qiu, S. Lin and X. Wang, *Adv. Mater.*, 2014, **26**, 805-809.
32. S. Yang, Y. Gong, J. Zhang, L. Zhan, L. Ma, Z. Fang, R. Vajtai, X. Wang and P. M. Ajayan, *Adv. Mater.*, 2013, **25**, 2452-2456.
33. X. C. Wang, K. Maeda, X. F. Chen, K. Takanabe, K. Domen, Y. D. Hou, X. Z. Fu and M. Antonietti, *J. Am. Chem. Soc.*, 2009, **131**, 1680-1681.
34. K. Schwinghammer, M. B. Mesch, V. Duppel, C. Ziegler, J. Senker and B. V. Lotsch, *J. Am. Chem. Soc.*, 2014, **136**, 1730-1733.
35. J. Hong, S. Yin, Y. Pan, J. Han, T. Zhou and R. Xu, *Nanoscale*, 2014, **6**, 14984-14990.
36. J. Zhang, Y. Wang, J. Jin, J. Zhang, Z. Lin, F. Huang and J. Yu, *Acs Appl. Mater. Inter.*, 2013, **5**, 10317-10324.
37. L. Ge, F. Zuo, J. Liu, Q. Ma, C. Wang, D. Sun, L. Bartels and P. Feng, *J. Phys. Chem. C*, 2012, **116**, 13708-13714.
38. S.-W. Cao, Y.-P. Yuan, J. Fang, M. M. Shahjamali, F. Y. C. Boey, J. Barber, S. C. Joachim Loo and C. Xue, *Int. J. Hydrogen. Energ.*, 2013, **38**, 1258-1266.
39. J. Fu, B. Chang, Y. Tian, F. Xi and X. Dong, *J. Mater. Chem. A*, 2013, **1**, 3083-3090.
40. X. Dai, M. Xie, S. Meng, X. Fu and S. Chen, *Appl. Catal. B-Environ.*, 2014, **158**, 382-390.
41. Z. Chen, S. Liu, M.-Q. Yang and Y.-J. Xu, *Acs Appl. Mater. Inter.*, 2013, **5**, 4309-4319.
42. F.-X. Xiao, J. Miao and B. Liu, *J. Am. Chem. Soc.*, 2014, **136**, 1559-1569.
43. N. Zhang, Y. Zhang, X. Pan, X. Fu, S. Liu and Y.-J. Xu, *J. Phys. Chem. C*, 2011, **115**, 23501-23511.
44. X. An, X. Yu, J. C. Yu and G. Zhang, *J. Mater. Chem. A*, 2013, **1**, 5158-5164.
45. J. Ran, J. Zhang, J. Yu, M. Jaroniec and S. Z. Qiao, *Chem. Soc. Rev.*, 2014, **43**, 7787-7812.
46. S. Chen, J. Duan, Y. Tang, B. Jin and S. Z. Qiao, *Nano Energy*, 2015, **11**, 11-18.
47. Y. Zheng, Y. Jiao, L. H. Li, T. Xing, Y. Chen, M. Jaroniec and S. Z. Qiao, *Acs Nano*, 2014, **8**, 5290-5296.
48. J. Hong, Y. Wang, Y. Wang, W. Zhang and R. Xu, *Chemsuschem*, 2013, **6**, 2263-2268.
49. L. Yin, Y.-P. Yuan, S.-W. Cao, Z. Zhang and C. Xue, *Rsc. Adv.*, 2014, **4**, 6127-6132.
50. J. Ran, J. Zhang, J. Yu and S. Z. Qiao, *Chemsuschem*, 2014, **7**, 3426-3434.
51. J. Zhang, L. Qi, J. Ran, J. Yu and S. Z. Qiao, *Adv. Energy Mater.*, 2014, **4**, 1301925.
52. W. Zhang, Y. Wang, Z. Wang, Z. Zhong and R. Xu, *Chem. Commun.*, 2010, **46**, 7631-7633.
53. X. Chen, J. Zhang, X. Fu, M. Antonietti and X. Wang, *J. Am. Chem. Soc.*, 2009, **131**, 11658-11659.
54. X. Wang, K. Maeda, A. Thomas, K. Takanabe, G. Xin, J. M. Carlsson, K. Domen and M. Antonietti, *Nat. Mater.*, 2009, **8**,

76-80.
55. L. Ge, C. Han and J. Liu, *J. Mater. Chem.*, 2012, **22**, 11843-11850.
56. L. Ge, C. Han, X. Xiao and L. Guo, *Int. J. Hydrogen. Energ.*, 2013, **38**, 6960-6969.
57. J. Yuan, J. Wen, Q. Gao, S. Chen, J. Li, X. Li and Y. Fang, *Dalton Trans.*, 2015, **44**, 1680-1689.
58. X. Lu, K. Xu, P. Chen, K. Jia, S. Liu and C. Wu, *J. Mater. Chem. A*, 2014, **2**, 18924-18928.
59. X. She, H. Xu, Y. Xu, J. Yan, J. Xia, L. Xu, Y. Song, Y. Jiang, Q. Zhang and H. Li, *J. Mater. Chem. A*, 2014, **2**, 2563-2570.
60. Q. Lin, L. Li, S. Liang, M. Liu, J. Bi and L. Wu, *Appl. Catal. B-Environ.*, 2015, **163**, 135-142.
61. X. Wang, X. Chen, A. Thomas, X. Fu and M. Antonietti, *Adv. Mater.*, 2009, **21**, 1609-+.
62. J. Yu, Y. Yu, P. Zhou, W. Xiao and B. Cheng, *Appl. Catal. B-Environ.*, 2014, **156–157**, 184-191.
63. K. Sing, D. Everett, R. Haul, L. Moscou, R. Pierotti, J. Rouquerol and T. Siemieniewska, *Pure Appl. Chem*, 1985, **57**, 603-619.
64. F. E. Osterloh, *Chem. Mater.*, 2007, **20**, 35-54.
65. Y. Hou, Y. Zhu, Y. Xu and X. Wang, *Appl. Catal. B-Environ.*, 2014, **156**, 122-127.
66. J. Yu, S. Wang, B. Cheng, Z. Lin and F. Huang, *Catal. Sci. Technol.*, 2013, **3**, 1782-1789.
67. X. Zong, J. Han, G. Ma, H. Yan, G. Wu and C. Li, *J. Phys. Chem. C*, 2011, **115**, 12202-12208.
68. J. Chen, X.-J. Wu, L. Yin, B. Li, X. Hong, Z. Fan, B. Chen, C. Xue and H. Zhang, *Angew. Chem. Int. Edit.*, 2015, **54**, 1210-1214.
69. S. C. Yan, Z. S. Li and Z. G. Zou, *Langmuir*, 2009, **25**, 10397-10401.
70. J. S. Zhang, X. F. Chen, K. Takanabe, K. Maeda, K. Domen, J. D. Epping, X. Z. Fu, M. Antonietti and X. C. Wang, *Angew. Chem. Int. Edit.*, 2010, **49**, 441-444.
71. Y. Zheng, Y. Jiao, Y. Zhu, L. H. Li, Y. Han, Y. Chen, A. Du, M. Jaroniec and S. Z. Qiao, *Nat. Commun.*, 2014, **5**, 3783.
72. J. Duan, S. Chen, M. Jaroniec and S. Z. Qiao, *Acs Nano*, 2015, **9**, 931-940.
73. Y. Jiao, Y. Zheng, M. Jaroniec and S. Z. Qiao, *Chem. Soc. Rev.*, 2015, DOI: 10.1039/C4CS00470A.
74. Y. Zheng, Y. Jiao, M. Jaroniec and S. Z. Qiao, *Angew. Chem. Int. Edit.*, 2015, **54**, 52-65.
75. J. Low, S. Cao, J. Yu and S. Wageh, *Chem. Commun.*, 2014, **50**, 10768-10777.